

Article

Open Access



Air-exposed lithium metal as a highly stable anode for low-temperature energy storage applications

Shumin Zheng¹, Haitao Geng¹, Svetlana N. Eliseeva^{2,*}, Bao Wang^{1,*}

¹State Key Laboratory of Biochemical Engineering, Institute of Process Engineering, Chinese Academy of Sciences, Beijing 100190, China.

²Department of Electrochemistry, Institute of Chemistry, Saint Petersburg State University, St. Petersburg 198504, Russia.

***Correspondence to:** Dr. Svetlana N. Eliseeva, Department of Electrochemistry, Institute of Chemistry, Saint Petersburg State University, Universitetskaya emb, 7/9, St. Petersburg 198504, Russia. E-mail: svetlana.eliseeva@spbu.ru; Prof. Bao Wang, State Key Laboratory of Biochemical Engineering, Institute of Process Engineering, Chinese Academy of Sciences, Beier 1, Haidian, Beijing 10019, China. E-mail: baowang@ipe.ac.cn

How to cite this article: Zheng S, Geng H, Eliseeva SN, Wang B. Air-exposed lithium metal as a highly stable anode for low-temperature energy storage applications. *Energy Mater* 2022;2:200042. <https://dx.doi.org/10.20517/energymater.2022.66>

Received: 23 Oct 2022 **First Decision:** 23 Nov 2022 **Revised:** 1 Dec 2022 **Accepted:** 6 Dec 2022 **Published:** 16 Dec 2022

Academic Editors: Yuping Wu, Sen Xin **Copy Editor:** Fangling Lan **Production Editor:** Fangling Lan

Abstract

The demand for cryogenic applications has resulted in higher requirements for the low-temperature performance of energy storage systems. Lithium-metal batteries are the most promising energy storage systems. Lithium-metal anodes have the merits of high capacity and low potential. However, at low temperatures, especially sub-zero, the formation of lithium dendrites seriously hinders their applications. Herein, distinct from the traditional strategies of separating lithium metal from oxygen substances, we propose a new strategy to suppress dendrites by exposing lithium metal to air for short periods to generate a controlled oxidative protective layer *in situ* that is compact, homogeneous and mainly composed of Li_3N , Li_2O , LiOH and Li_2CO_3 . Symmetrical and full cells are assembled. The air-pretreated Li metal symmetrical cell exhibits an excellent lifespan of up to 4500 h (1 mA cm^{-2}) at 30°C and also shows a smaller voltage polarization of 20 mV at 1.0 mA cm^{-2} at -20°C . Importantly, the full cell using the air-pretreated Li metal as an anode and NCM811 as a cathode can charge-discharge normally at -20 and -40°C . This work provides an efficient and facile approach for developing superior lithium-metal batteries for future utilization at a wide range of temperatures.

Keywords: Lithium-metal batteries, lithium dendrites, *in-situ* self-assembly, air-pretreated layer, protective layer



© The Author(s) 2022. **Open Access** This article is licensed under a Creative Commons Attribution 4.0 International License (<https://creativecommons.org/licenses/by/4.0/>), which permits unrestricted use, sharing, adaptation, distribution and reproduction in any medium or format, for any purpose, even commercially, as long as you give appropriate credit to the original author(s) and the source, provide a link to the Creative Commons license, and indicate if changes were made.



INTRODUCTION

Lithium-metal batteries (LMBs) are considered to be the most promising candidates for next-generation electrochemical energy storage technology, attributed to their merits, which include the high capacity (3860 mAh g^{-1}) and low potential (-3.04 V vs. standard hydrogen electrode) of the lithium-metal anode. Uncontrollable dendrite growth, significant volume changes during cycling and repeated formation of the solid electrolyte interface (SEI) are the bottlenecks of LMBs. To address these issues, many efforts have been devoted to stabilizing the SEI interface and suppressing dendrite growth, such as surface protection layers^[1], three-dimensional hosts^[2], artificial SEIs^[3] and electrolyte engineering^[4]. The majority of these efforts have been dedicated to room-temperature conditions^[5-8]. To advance the practical application of LMBs, their performance at low temperatures has attracted more attention as energy storage systems are expected to operate or store under sub-zero environmental conditions. However, the instinct problems of dendrite formation and growth will be aggravated certainly at low temperatures, leading to the large formation of dead Li, safety issues and short lifespans^[9]. On this basis, a more efficient strategy should be introduced to suppress dendrite formation and growth at low temperatures. Regarding highly efficient dendrite-suppressing strategies at room temperature, the construction of surface protection layers has been studied extensively. Powders, fibers and films have been attached to the surface of Li metal by rolling, sputtering or deposition^[10-12]. However, the interfaces between Li metal and protection layers or SEI can make the mechanical durability weak^[13]. Importantly, the cost will limit the practical applications of the above strategies and extra materials and procedures will be introduced and added to construct a surface protection layer/artificial SEI. Therefore, there is a strong demand for facile and low-cost technology to construct robust layers/SEIs to suppress dendrites at low temperatures.

The main components of a SEI are lithium-based compounds, such as LiF, Li_2CO_3 , LiOH, Li_2O and Li_3N ^[14]. Typically, the SEI compositions are highly dependent on the additives in the electrolyte, such as LiNO_3 , fluoroethylene carbonate, H_2O and CO_2 , which are added to regulate metallic Li deposition^[15]. Nevertheless, these additives are continuously consumed and exhausted rapidly because their solubility in the widely applied carbonate electrolytes is low^[16]. For low-temperature applications, inspired by the merits of the surface protection layer and artificial SEI, we exposed Li metal directly to air and an air-pretreated layer (APL) formed on the surface. Li metal can directly/indirectly react with N_2 , O_2 , H_2O and CO_2 and form lithium-based compounds (Li_3N , Li_2O , LiOH and Li_2CO_3), which are the main components of the SEI. These *in situ* formed compounds guarantee the strong adhesion between Li metal and the APL, as well as the interactions between the components in the APL. Among the formed compounds, Li_3N can function as a Li^+ conductor ($10^{-3} \text{ S cm}^{-1}$)^[17,18], the density functional theory-calculated Young's moduli of Li_2CO_3 is 36.2 GPa ^[19], which can help to avoid the damage to the APL and Li_2O buffers the direct contact of unstable Li_2CO_3 from Li metal during cycling^[20]. Finally, an *in situ* stable dense passivation protection layer formed on the Li metal surface and the lithium-rich compounds that exist in the layer have a synergistic effect blocking the direct contact of naked Li and the electrolyte and preventing electron tunneling without sacrificing extra electrolyte. Importantly, the extremely low cost and facile merits of this strategy are particularly attractive for practical applications.

The performance of LMBs must be sensitive to the exposure time in air because the thickness of the protective layer increases with exposure time; thus, the thickness of the APL should be a balance of resistivity and conductivity. Thus, the main problem is controlling the exposure time. Li metal is treated in air with a humidity of $\sim 40\%$ for 10 min, 30 min, 1 h and 2 h, respectively. We then evaluated their electrochemical performance at both room ($30 \text{ }^\circ\text{C}$) and low temperatures (-20 and $-40 \text{ }^\circ\text{C}$).

RESULTS AND DISCUSSION

As depicted in [Figure 1A](#), when exposed to air, the highly active Li metal reacts with N_2 , O_2 , H_2O and CO_2 directly/indirectly and then the APL forms on the surface of the Li metal^[21]. [Figure 1B](#) shows the X-ray diffraction (XRD) for pure Li, Li-10 min, Li-30 min, Li-1 h and Li-2 h. The XRD peaks 36.19° , 51.97° and 87.89° of pure Li are corresponding to the (110), (200) and (220) facets (JCPDS No. 15-0401), respectively. After exposing Li metal to the air, with increasing exposure time, the peaks of pure Li became weakened gradually, while the peaks of Li compounds became stronger and stronger. The weak peak of the Li_2O (111) facet at 33.61° was observed in Li-30 min, Li-1 h and Li-2 h, indicating the existence of Li_2O , which may locate underneath the formed layer and direct contact with Li metal. There are two peaks at $\sim 32.00^\circ$, the peak at 32.48° is the (101) facet of LiOH and the peak at 32.53° is the (200) facet of Li_3N . The Li_3N (200) peak appears first, then the LiOH (101) peak becomes stronger gradually with increasing exposure time and the same applies to the two peaks at $\sim 36.00^\circ$. Finally, the peaks of LiOH and Li_2CO_3 became the most obvious among the formed compounds and it can be inferred that LiOH and Li_2CO_3 exist at the outermost region of the APL. Li_3N should be located in the middle or interior of the APL because Li_3N is unstable in air. In addition, Li_2CO_3 can react with Li metal under the internal operating conditions of the battery^[20]. The possible distribution of the lithium-based compounds in the protection layer is shown in [Figure 1A](#).

To obtain the morphological variations of the APL on Li metal, the surface was observed through scanning electron microscopy (SEM) analysis [[Figure 1C-G](#)]. The surface of pure Li metal is a relative plane and with increasing exposure time, the surface becomes rougher with raised bulges observed in the zoomed-in area. The enriched cracks indicate the formation of a large amount of lithium-based compounds, because the molecular volumes (cell volume) of Li_3N , Li_2O , LiOH and Li_2CO_3 are 44.88, 25.27, 56.89 and 122.9 \AA^3 , respectively, and that of a Li atom is 42.9 \AA^3 . The molecular volumes of Li_3N , LiOH and Li_2CO_3 are larger than that of a single lithium atom. Therefore, with the accumulation of these compounds on the Li metal substrate, the inner stress of the APL increases, cracks appear and the APL of Li-1 h and Li-2 h tends to peel off. As shown in the digital photos in the insets of [Figure 1C-G](#), the pure Li metal has a bright metallic luster, the majority of the Li-10 min surface becomes dark with indistinct metallic Li, while the surface colors of Li-30 min, Li-1 h and Li-2 h are darkened. The uniform distribution of O, C and N within the APL was confirmed by the elemental characterization [[Figure 1H](#)].

To further investigate the components of the APL, we performed high-resolution transmission electron microscopy (HRTEM) tests [[Figure 2A-I](#)] to reveal that the APL mainly contained nanocrystals of lithium-based compounds. The crystalline grains were identified. The lattice fringe with the interplanar spacing of 0.265 nm was identified to be the (111) crystal plane of Li_2O and the (110) and (102) crystal planes of LiOH with interplanar spacings of 0.251 and 0.186 nm, respectively, were observed. The lattice fringes with the interplanar spacings of 0.320 and 0.392 nm were identified to be (110) and (102) crystal planes of Li_3N , respectively, and the (-221), (-110), (-220), (200) and (-311) crystal planes of Li_2CO_3 were observed with the corresponding interplanar spacings of 0.211, 0.209, 0.431, 0.376 and 0.240 nm, respectively. The polycrystalline nature of the APL was also verified by selected area electron diffraction (SAED), as shown in [Figure 2J](#), with the diffraction rings ascribed to (-220) Li_2CO_3 , (211) LiOH, (212) LiOH and (422) Li_2O . The chemical composition of the APL was also obtained by X-ray photoelectron spectroscopy (XPS). [Figure 2K-M](#) show the Li 1s, C 1s and O 1s X-ray photoelectron spectra of APL, respectively. The results also confirm the existence of Li_2O , Li_3N , LiOH and Li_2CO_3 . The peaks at 54.0, 54.9 and 55.2 eV of Li 1s can be ascribed to Li_2O , LiOH and Li_2CO_3/Li_3N , respectively. The peak of C 1s at 284.8 eV is the hydrocarbon and the peak at 289.7 eV is Li_2CO_3 . In addition, other species of Li were detected at 286.3 eV, which could be $ROCO_2Li$ ^[21].

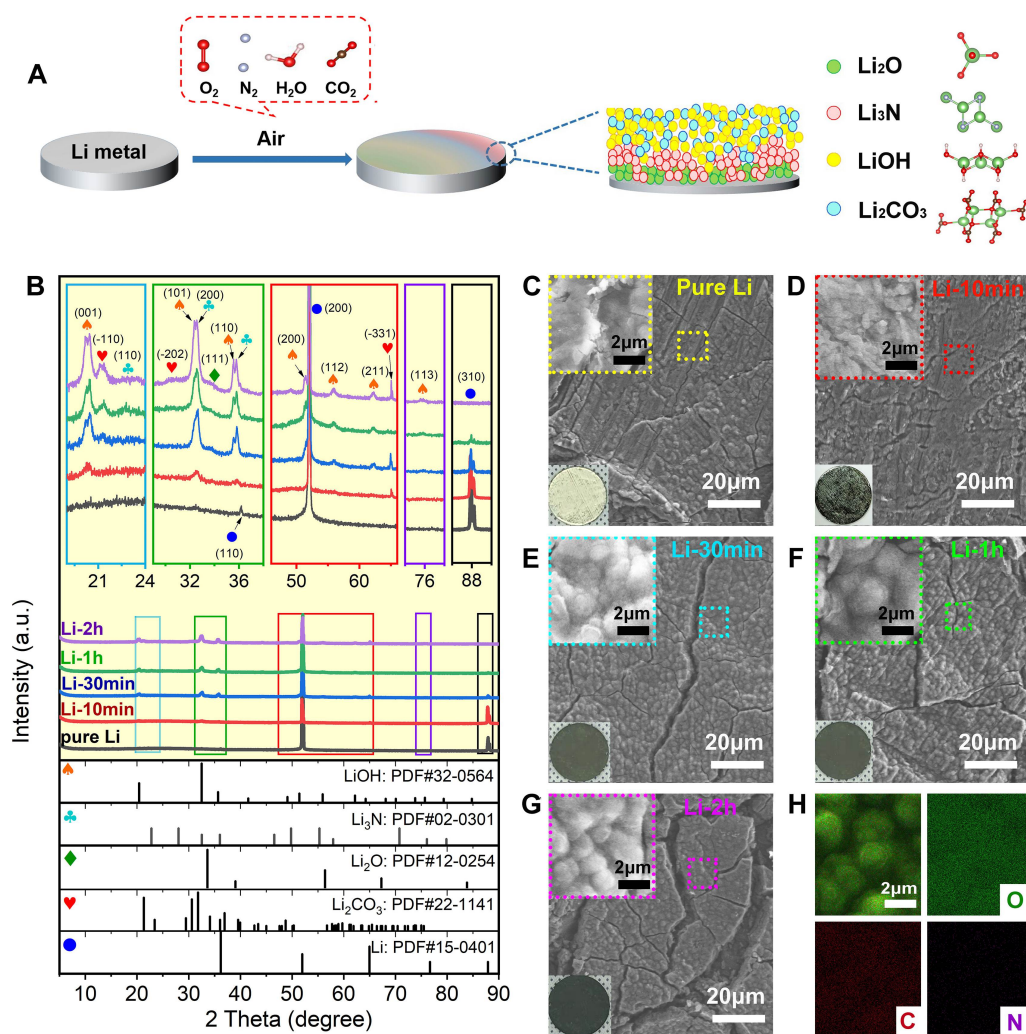


Figure 1. (A) Schematic synthesis of *in-situ* protection layer on lithium metal through exposure to air. (B) X-ray diffraction pattern of pure Li, Li-10 min, Li-30 min, Li-1 h and Li-2 h. SEM images of (C) pure Li, (D) Li-10 min, (E) Li-30 min, (F) Li-1 h and (G) Li-2 h. Insets show high-magnification images and digital photographs. (H) EDX mapping of *in-situ* protection layer.

Based on the above characterization, although the components of the *in-situ* APL have been revealed, it is also meaningful to confirm its dendrite suppression ability. First, the electrochemical performance was evaluated carefully at room temperature [Figure 3] using symmetrical cells. The initial electrochemical impedance spectroscopy (EIS) results reveal the low conductivity of APL [Figure 3A], with charge transfer resistance (R_{ct}) values of 60, 420, 900, 2720 and 6294 Ω for pure Li, Li-10 min, Li-30 min, Li-1 h and Li-2 h, respectively. The R_{ct} increased drastically with the exposure time. The EIS plots after cycling (1st, 2nd, 5th, 10th, 20th, 50th and 100th) were acquired, with the R_{ct} value tending to reduce with cycling, as shown in Figure 3B. The R_{ct} of all samples decreased beneath 200 Ω after the 1st cycle, which could be due to the uniform deposition of Li metal in the APL after cycling. Conductive pathways were then constructed, revealing that the electrochemical performance was only partially determined by the initial resistance. Figure 3C and D show the Tafel plots for evaluating the exchange current density. Pure Li exhibits the largest exchange current density; after cycling, the value of all samples tends to increase, which corresponds to the EIS results. The above data reveal that the conductivity of the APL was enhanced after cycling.

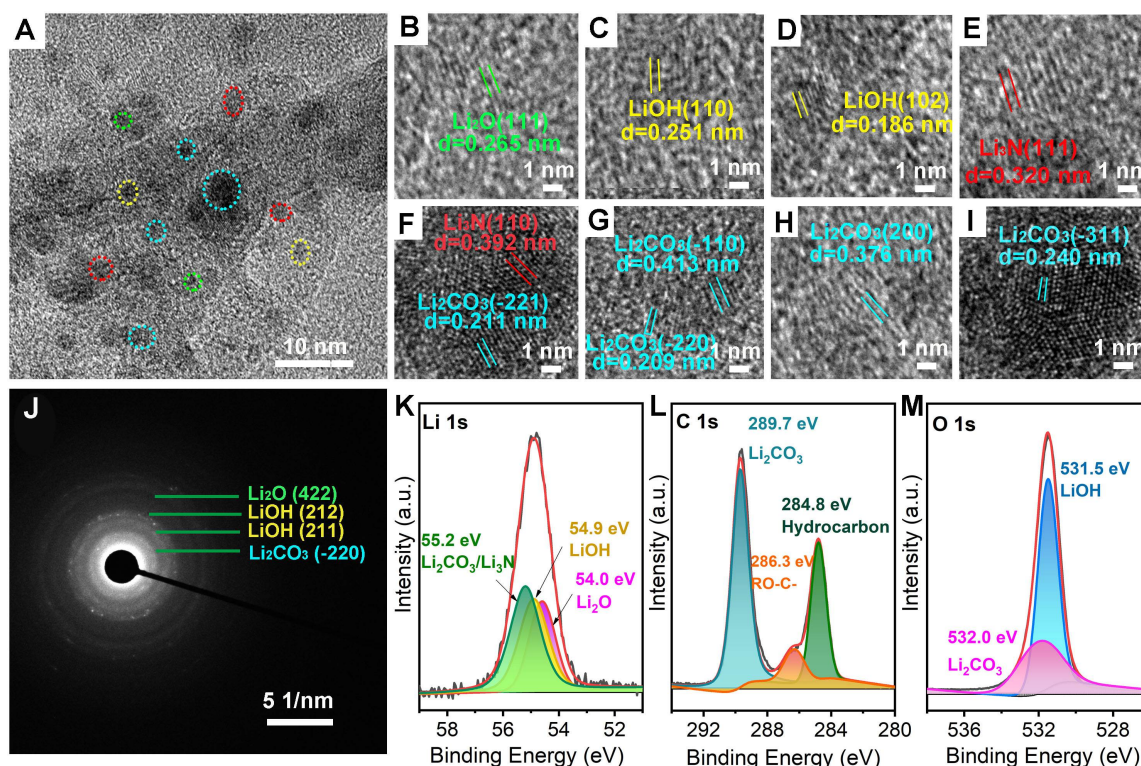


Figure 2. (A) TEM image, (B-I) HRTEM images, (J) SAED and XPS spectra of *in-situ* protection layer. XPS spectra of (K) Li 1s, (L) C 1s and (M) O 1s.

Figure 3E shows the voltage profiles of the symmetrical cells during Li plating and stripping with increasing current densities of 1, 2, 3, 5 and 10 mA cm⁻² at a fixed capacity of 1 mAh cm⁻². Li-10 min exhibits almost the same plots as pure Li but with a larger voltage range. With the exposure time increasing to greater than or equal to 30 min, the voltage range was kept in the range of -50-50 mV at 1 mA cm⁻². Among all the samples, Li-30 min exhibited the best voltage control ability and when the current density switched to 10 mA cm⁻², the voltage fluctuation range could still be maintained at -100-100 mV. The ultralong lifespan of up to 4500 h of Li-30 min at the current density of 10 mA cm⁻² is shown in Figure 3F. Pure Li has a short circuit at ~240 h (120 cycles) and the voltage of Li-1 h and Li-2 h was unstable. The selected stripping-plating curves in Figure 3F further reveal the excellent dendrite suppression ability of the APL. To observe the stripping-plating behavior of the APL more intuitively, liquid cell tests were employed with digital images of the Li/Li-30 min stripping-plating at the current density of 1 mA cm⁻² shown in Figure 3G. Bunches of dendrites were formed on the surface of pure Li metal with dots of Li metal observed on the Li-30 min surface. The SEM images of the pure Li surface after short circuit (120 cycles) are shown in Figure 3H, with a typical dendrite morphology observed. As shown in Figure 3I, the surface of Li-30 min after 120 cycles shows that no dendrites or round particles formed; as the cycling time increased to 2000 h (1000 cycles), a dendrite-like structure was observed [Figure 3J], but the end was round [Figure 3K], this corresponds to the conclusion that the Li nucleation and early growth is critical to the final deposition morphology^[22]. The above analysis reveals the excellent suppression and morphology-controlling ability of the *in-situ* APL on dendrites.

As four main Li compounds were detected, it is therefore imperative to test the dendrite-suppression performance of each compound. Li₃N, Li₂O, LiOH, and Li₂CO₃ were applied to modify Li metal by cold

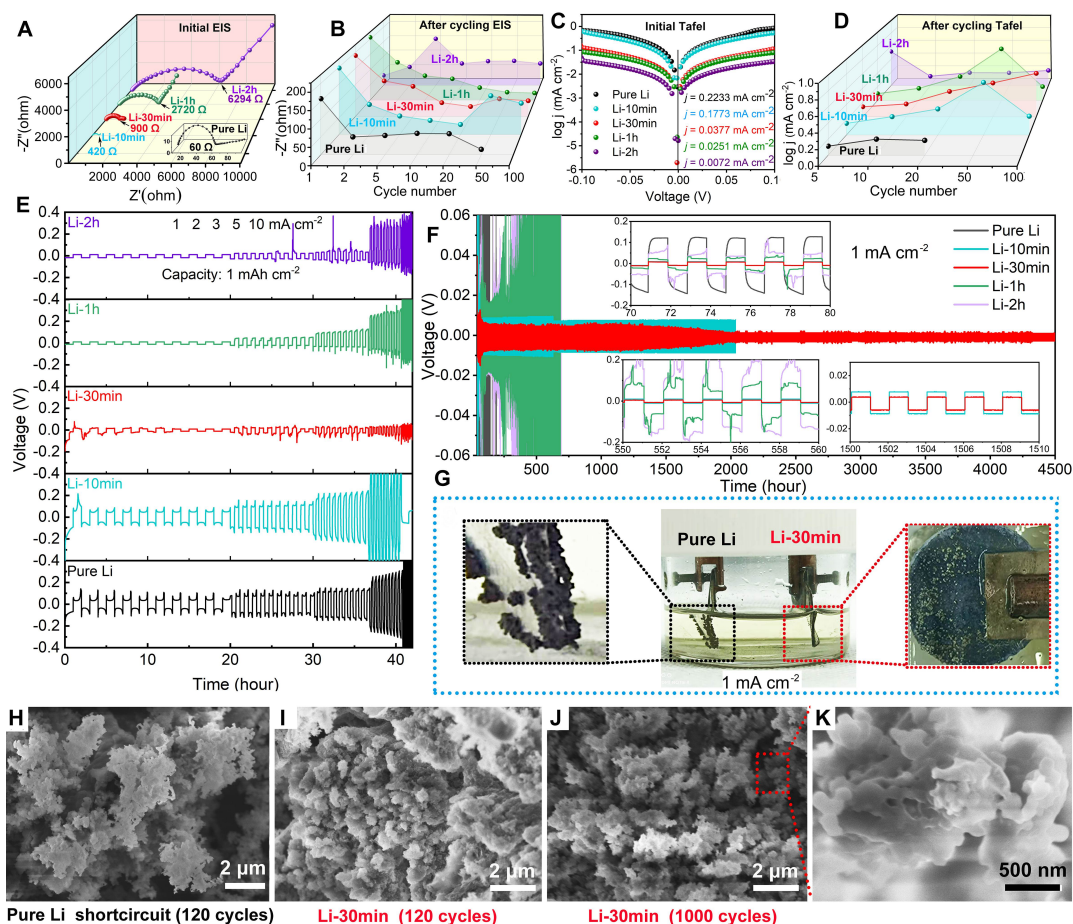


Figure 3. (A) EIS plots, (B) Rct variations after cycling, (C) Tafel plots and (D) exchange current density variations after cycling of pure Li, Li-10 min, Li-30 min, Li-1 h and Li-2 h. (E) Corresponding voltage-time profiles of Li plating/stripping at current densities of 1, 2, 3, 5 and 10 mA cm^{-2} in symmetrical cells. (F) Long cycling voltage-time profiles at 1 mA cm^{-2} . Insets show selected voltage-time profiles. (G) Digital images of liquid cell tests for Li/Li-30 min stripping-plating at a current density of 1 mA cm^{-2} . (H) SEM image of pure Li surface after 120 cycles in symmetrical cell. (I) SEM image of Li-30 min surface after 120 cycles in symmetrical cell. (J and K) SEM images of Li-30 min surface after 1000 cycles in symmetrical cell. All tests were performed at 30 °C.

pressing. Their voltage profiles during Li plating and stripping with increasing current densities of 1, 2, 3, 5 and 10 mA cm^{-2} at a fixed capacity of 1 mAh cm^{-2} are shown in [Supplementary Figure 1](#). Among them, Li_2O and LiOH exhibit better dendrite suppression, together with the good mechanical performance of Li_2CO_3 and superior ion conductivity of Li_3N , thereby enabling a synthetic effect.

The energy storage performance of Li-30 min|NCM811_{img} and pure Li|NCM811_{img} cells was determined at 30, -20 and -40 °C [1.0 M LiPF_6 in EC:DEC (1:1 v/v) as the electrolyte]. The voltage of pure Li symmetrical cell reaches ~500 mV at 1 mA cm^{-2} at -20 °C and has a short circuit after 70 h. The corresponding voltage of the Li-30 min symmetrical cell is ~20 mV [Figure 4A]. The Li-30 min symmetrical cell shows stable Li plating-stripping for more than 500 h and exhibits excellent dendrite suppression at low temperatures [Figure 4B]. Under 30 °C [Supplementary Figure 2], the capacities of Li-30 min|NCM811_{img} at 0.1 C, 0.2 C, 0.5 C, 1.0 C, 2.0 C, 5.0 C and 10.0 C are 208, 205, 196, 184, 140, 100 and 41 mAh g^{-1} , respectively, while those of pure Li|NCM811_{img} are 173, 154, 146, 137, 117, 93 and 54 mAh g^{-1} , respectively, Li-30 min|NCM811_{img}, respectively, exhibiting higher capacity compared to pure Li|NCM811_{img}. This is because the APL of Li-30 min provides the required components for the SEI, while the extra capacity cost to generate the continuous

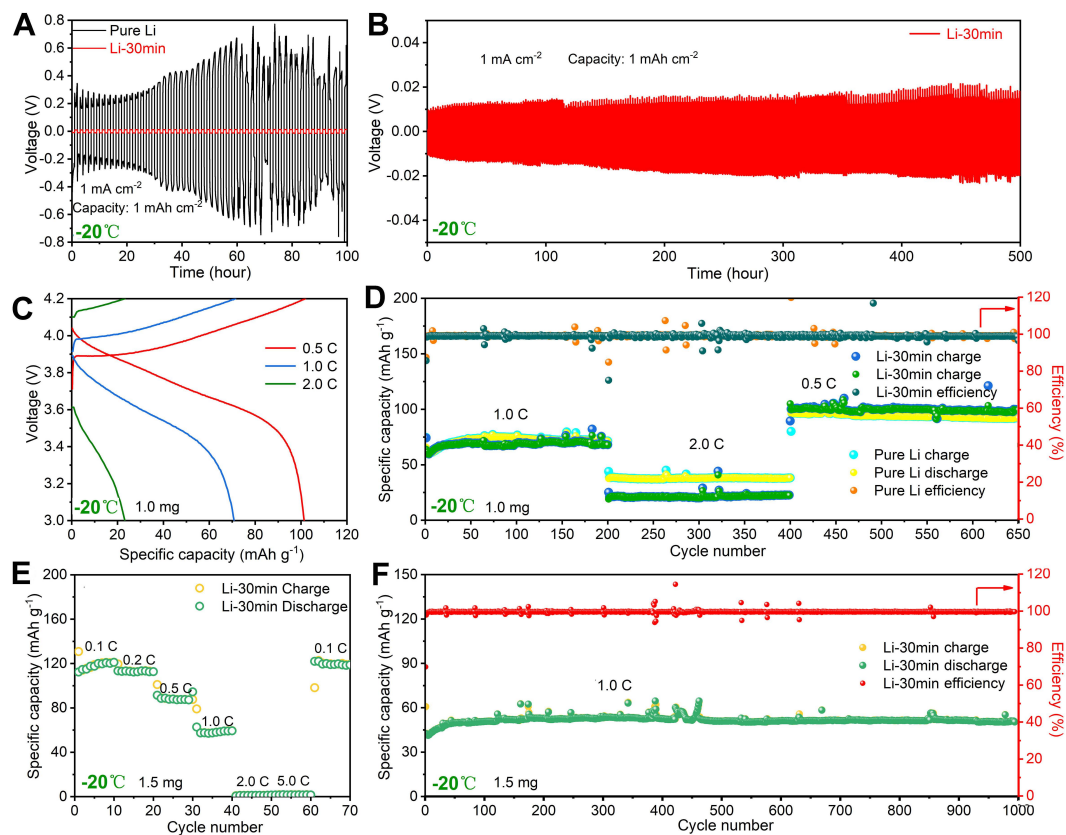


Figure 4. (A) Voltage-time profiles of Li-30 min and pure Li symmetrical cells. (B) Long cycling voltage-time profiles at 1 mA cm^{-2} . (C) Charge-discharge profiles of Li-30 min full cell with 1 mg of NCM811. (D) Rate and cycling performance of Li-30 min and pure Li with 1 mg of NCM811. (E) Rate and (F) cycling performance of Li-30 min and pure Li with 1.5 mg of NCM811. All tests were performed at $-20 \text{ }^{\circ}\text{C}$.

formation SEI films in pure Li|NCM811_{1mg}, but at 10 C, the capacity of pure Li|NCM811_{1mg} becomes higher due to the inferior conductivity of the APL on Li-30 min hindering the formation of smooth Li. As a result, the APL performs well at low rates. At $30 \text{ }^{\circ}\text{C}$ [Supplementary Figure 3], a long cycling (300 cycles) test was performed, with the per cycle capacity decay of Li-30 min|NCM811_{1mg} being 0.05%, while that of pure Li|NCM811_{1mg} is 0.12%.

The charge-discharge curves of Li-30 min|NCM811_{1mg} at 30, -20 and $-40 \text{ }^{\circ}\text{C}$ are shown in Supplementary Figure 4, Figure 4C and Supplementary Figure 5, exhibiting sluggish dynamics and charge-discharge capacity decreases at reduced temperatures. Figure 4D shows the cycling performance of Li-30 min|NCM811_{1mg} and pure Li|NCM811_{1mg} at different rates at $-20 \text{ }^{\circ}\text{C}$, 200 cycles at 1.0 C, 200 cycles at 2.0 C and 250 cycles at 0.5 C. The corresponding capacities of Li-30 min|NCM811_{1mg} are 70, 23 and 100 mAh g^{-1} , respectively, while those of pure Li|NCM811_{1mg} are 72, 38, and 92 mAh g^{-1} , respectively. At 2.0 C, Li-30 min|NCM811_{1mg} exhibits lower capacity, which shows the same trend as that at $30 \text{ }^{\circ}\text{C}$, but due to the sluggish dynamic at $-20 \text{ }^{\circ}\text{C}$, the rate performance is inferior. Nevertheless, Li-30 min|NCM811_{1mg} shows the advantage at small current densities; at 0.5 C, its capacity is higher than that of pure Li|NCM811_{1mg}. In addition, the per cycle capacity decay at 0.5 C of Li-30 min|NCM811_{1mg} is nearly zero, while that of pure Li|NCM811_{1mg} is 0.02%. The rate and cycling performances of Li-30 min|NCM811_{1.5mg} and pure Li|NCM811_{1.5mg} were evaluated at $-20 \text{ }^{\circ}\text{C}$. The capacities at 0.1 C, 0.2 C, 0.5 C and 1.0 C are 120, 113, 88 and 60 mAh g^{-1} , respectively, and the capacity recovered to 120 mAh g^{-1} when current density switched back to

0.1 C [Figure 4E], reflecting good reversibility. As shown in Figure 4F, Li-30 min|NCM811_{1.5mg} exhibits excellent cycling stability under -20 °C; after 1000 cycles at 1.0 C, the capacity maintains at ~51 mAh g⁻¹ without decay. The rate and cycling performances were further investigated under -40 °C, as shown in Supplementary Figures 6 and 7. The capacities of Li-30 min|NCM811_{1mg} at 0.05 C, 0.1 C and 0.2 C are 95, 66 and 30 mAh g⁻¹, respectively. Li-30 min|NCM811_{1mg} is unable to charge-discharge when current increases over 0.5 C and the corresponding capacities of pure Li|NCM811_{1mg} are 53, 47 and 0.3 mAh g⁻¹, respectively. The cycling performance at 0.1 C (100 cycles) and 0.2 C (50 cycles) indicates the good stability of Li-30 min|NCM811_{1mg}. In addition, the charge-discharge efficiency is lower at -40 °C.

CONCLUSION

Exposing pure Li to air alters the Li deposition behavior and enables the dendrite-free growth of Li metal at moderate current densities, thereby enhancing the cycling stability and extending the cycle life for high-capacity Li metal batteries at a wide temperature range. In contrast to typical efforts made to protect Li metal from oxidation, we exposed Li to air and made it oxidize. This strategy has the advantages of being extremely low cost, green and has been shown to be applicable to various metal batteries (e.g., Na-, K- and Zn-metal batteries) at wide temperatures.

Experimental section

Materials: Lithium oxide (Li₂O, 99.99%, Aladdin), lithium nitride (Li₃N, 99.9%, Aladdin), lithium carbonate (Li₂CO₃, 99.5%, Macklin) and lithium hydroxide (LiOH, 99%, J&K). All chemicals were used as received.

Preparation of air-pretreated Li metal: Li metal was exposed to air (humidity of 40%). Four samples were then obtained and all samples were named according to their air exposure time, which are Li-10 min, Li-30 min, Li-1 h and Li-2 h.

Structural characterization: X-ray diffraction (XRD) patterns were obtained by using an X'Pert PRO MDP with Cu K α radiation ($\lambda = 1.5405 \text{ \AA}$) with 40 mA and 40 kV. X-ray photoelectron spectroscopy (XPS) was collected at an Escalab 250Xi spectrophotometer. Field emission scanning electron microscopy (FESEM) images were obtained using a JEOL JSM-7001F scanning electron microscope operating at 15 kV. Transmission electron microscopy (TEM) images were obtained using a JEOL JEM-2100F electron microscope operating at 200 kV. Thermogravimetric analysis (TGA) data were collected using a DTA-60 (Shimadzu), annealed under air/N₂ atmosphere at 10 °C min⁻¹.

Electrochemical measurements: The CR2032 coin-type cells were assembled in an argon-filled glove box. The electrolyte consisted of a solution of 1.0 M LiPF₆ in EC:DEC (1:1 v/v) and the amount of electrolyte used for the batteries was 40 μ L. The cells were cycled galvanostatically in the voltage range of 3.0-4.2 V with a battery testing system (Neware Electronic Co., China). Electrochemical impedance spectroscopy (EIS) was conducted by a bio-logic VMP3 electrochemical workstation.

DECLARATIONS

Authors' contributions

Completing the experiments and preparing the manuscript draft: Zheng S

Discussing and revising the manuscript: Geng H, Eliseeva SN

Writing-review and editing, funding acquisition, supervision: Wang B

Availability of data and materials

Not applicable.

Financial support and sponsorship

We acknowledge financial support from National Natural Science Foundation of China (No. 52172250).

Conflicts of interest

All authors declared that there are no conflicts of interest.

Ethical approval and consent to participate

Not applicable.

Consent for publication

Not applicable.

Copyright

© The Author(s) 2022.

REFERENCES

1. Xu H, Li Y, Zhou A, et al. Li₃N-modified garnet electrolyte for all-solid-state lithium metal batteries operated at 40 °C. *Nano Lett* 2018;18:7414-8. [DOI](#) [PubMed](#)
2. Wang SH, Yin YX, Zuo TT, et al. Stable Li metal anodes via regulating lithium plating/stripping in vertically aligned microchannels. *Adv Mater* 2017;29:1703729. [DOI](#) [PubMed](#)
3. Ji X, Hou S, Wang P, et al. Solid-state electrolyte design for lithium dendrite suppression. *Adv Mater* 2020;32:e2002741. [DOI](#) [PubMed](#)
4. Hu Z, Li G, Wang A, Luo J, Liu X. Recent progress of electrolyte design for lithium metal batteries. *Batteries Supercaps* 2020;3:331-5. [DOI](#)
5. Bi Z, Guo X. Solidification for solid-state lithium batteries with high energy density and long cycle life. *Energy Mater* 2022;2:200011. [DOI](#)
6. Meyerson ML, Papa PE, Heller A, Mullins CB. Recent developments in dendrite-free lithium-metal deposition through tailoring of micro- and nanoscale artificial coatings. *ACS Nano* 2021;15:29-46. [DOI](#) [PubMed](#)
7. Wondimkun ZT, Tegegne WA, Shi-kai J, et al. Highly-lithiophilic Ag@PDA-GO film to suppress dendrite formation on Cu substrate in anode-free lithium metal batteries. *Energy Stor Mater* 2021;35:334-44. [DOI](#)
8. Xiao Y, Xu R, Xu L, Ding J, Huang J. Recent advances in anion-derived SEIs for fast-charging and stable lithium batteries. *Energy Mater* 2022;1:100013. [DOI](#)
9. Gupta A, Manthiram A. Designing advanced lithium-based batteries for low-temperature conditions. *Adv Energy Mater* 2020;10:2001972. [DOI](#) [PubMed](#) [PMC](#)
10. Liu F, Wang L, Zhang Z, et al. A mixed lithium-ion conductive Li₂S/Li₂Se protection layer for stable lithium metal anode. *Adv Funct Mater* 2020;30:2001607. [DOI](#)
11. Wang D, Liu Y, Li G, Qin C, Huang L, Wu Y. Liquid metal welding to suppress Li dendrite by equalized heat distribution. *Adv Funct Mater* 2021;31:2106740. [DOI](#)
12. Luo Y, Li T, Zhang H, et al. Endogenous symbiotic Li₃N/cellulose skin to extend the cycle life of lithium anode. *Angew Chem Int Ed* 2021;60:11718-24. [DOI](#)
13. Liu S, Xia X, Deng S, et al. In Situ solid electrolyte interphase from spray quenching on molten Li: a new way to construct high-performance lithium-metal anodes. *Adv Mater* 2019;31:e1806470. [DOI](#) [PubMed](#)
14. Wu J, Ihsan-ul-haq M, Chen Y, Kim J. Understanding solid electrolyte interphases: advanced characterization techniques and theoretical simulations. *Nano Energy* 2021;89:106489. [DOI](#)
15. Zhang H, Luo J, Qi M, et al. Enabling lithium metal anode in nonflammable phosphate electrolyte with electrochemically induced chemical reactions. *Angew Chem Int Ed* 2021;60:19183-90. [DOI](#) [PubMed](#)
16. Fu L, Wang X, Wang L, et al. A salt-in-metal anode: stabilizing the solid electrolyte interphase to enable prolonged battery cycling. *Adv Funct Mater* 2021;31:2010602. [DOI](#)
17. Ma G, Wen Z, Wu M, et al. A lithium anode protection guided highly-stable lithium-sulfur battery. *Chem Commun* 2014;50:14209-12. [DOI](#) [PubMed](#)
18. Park K, Goodenough JB. Dendrite-suppressed lithium plating from a liquid electrolyte via wetting of Li₃N. *Adv Energy Mater* 2017;7:1700732. [DOI](#)

19. Zhai P, Liu L, Gu X, Wang T, Gong Y. Interface engineering for lithium metal anodes in liquid electrolyte. *Adv Energy Mater* 2020;10:2001257. [DOI](#)
20. Han B, Zhang Z, Zou Y, et al. Poor stability of Li_2CO_3 in the solid electrolyte interphase of a lithium-metal anode revealed by cryo-electron microscopy. *Adv Mater* 2021;33:e2100404. [DOI](#)
21. Zhang Y, Wang W, Tang H, et al. An ex-situ nitridation route to synthesize Li_3N -modified Li anodes for lithium secondary batteries. *J Power Sources* 2015;277:304-11. [DOI](#)
22. Guan X, Wang A, Liu S, et al. Controlling nucleation in lithium metal anodes. *Small* 2018;14:e1801423. [DOI](#) [PubMed](#)